

**Extraordinary anisotropic magnetoresistance in  $\text{CaMnO}_3/\text{CaIrO}_3$  heterostructures**Megha Vagadia,<sup>1</sup> Suman Sardar,<sup>1</sup> Tejas Tank,<sup>1</sup> Sarmistha Das,<sup>2</sup> Brandon Gunn,<sup>2</sup> Parul Pandey,<sup>3</sup> R. Hübner,<sup>3</sup> Fanny Rodolakis,<sup>4</sup> Gilberto Fabbris,<sup>4</sup> Yongseong Choi,<sup>4</sup> Daniel Haskel,<sup>4</sup> Alex Frano,<sup>2</sup> and D. S. Rana<sup>1,\*</sup><sup>1</sup>*Department of Physics, Indian Institute of Science Education and Research Bhopal, Madhya Pradesh 462066, India*<sup>2</sup>*Department of Physics, University of California, San Diego, California 92093, USA*<sup>3</sup>*Institute of Ion Beam Physics and Materials Research, Helmholtz-Zentrum Dresden-Rossendorf, 01328 Dresden, Germany*<sup>4</sup>*Advanced Photon Source, Argonne National Laboratory, Argonne, Illinois 60439, USA* (Received 21 January 2021; revised 4 November 2021; accepted 15 December 2021; published 3 January 2022)

The realization of fourfold anisotropic magnetoresistance (AMR) in  $3d$ - $5d$  heterostructures has boosted major efforts in antiferromagnetic (AFM) spintronics. However, despite the potential of incorporating strong spin-orbit coupling, only small AMR signals have been detected thus far, prompting a search for mechanisms to enhance the signal. In this paper, we demonstrate an extraordinarily elevated fourfold AMR of 70% realized in  $\text{CaMnO}_3/\text{CaIrO}_3$  thin film superlattices. We find that the biaxial magnetic anisotropy and the spin-flop transition in a nearly Mott insulating phase form a potent combination, each contributing one order of magnitude to the total signal. Dynamics between these phenomena capture a subtle interaction of pseudospin coupling with the lattice and external magnetic field, an emergent phenomenon creating opportunities to harness its potential in AFM spintronics.

DOI: [10.1103/PhysRevB.105.L020402](https://doi.org/10.1103/PhysRevB.105.L020402)

The recent emergence of antiferromagnetic (AFM) spintronics over its ferromagnetic (FM) counterpart is inspired by several advantages such as lack of stray fields, low operational power, and ultrafast control of the staggered spins at terahertz frequencies. An AFM spintronic device uses the phenomena of current-induced spin-orbit torque and anisotropic magnetoresistance (AMR) for data writing and reading operations [1–6]. The ongoing efforts in AMR aim to design heterostructures wherein one of its constituents possesses pronounced spin-orbit coupling (SOC) and magnetocrystalline anisotropies. A coupling of the magnetic field and weak magnetic moments of the canted AFM phase allows these anisotropies to manifest as anisotropic transport. A host of such functionalities are being realized in  $3d$ - $5d$  oxide heterostructures [7–13]. Epitaxial superlattices of iridium oxides ( $\text{Ca}/\text{SrIrO}_3$ ) having large SOC and electron-correlation-dominated  $3d$  oxides, for example, exhibit emergent magnetic and topological properties wherein the AMR is traced to the anisotropies in their magnetic order [12,13].

The nonmagnetic ground state of Ir pseudospin moments ( $J_{\text{eff}} = \frac{1}{2}$ ) in  $\text{SrIrO}_3$  and  $\text{CaIrO}_3$  is defined by the intricate interplay of SOC and electron correlations ( $U$ ) [7–10]. Tilting the balance of these energetics alters their ground state. For instance, lowering the dimensionality in epitaxial engineered thin films increases the  $U$  and induces pseudospin-based emergent magnetism. AMR in these iridate heterostructures is pinned to magnetic anisotropies underneath such that uniaxial and biaxial symmetries translate into twofold and fourfold AMR oscillations, respectively. The latter is preferred due to the larger number of sensitive nodes relevant in efficient data

readout. The large-bandwidth  $\text{SrIrO}_3$  interfaced with magnetic or nonmagnetic  $3d$  systems yields two- and fourfold AMR attributed to a variety of magnetic phases, interface coupling, charge-transfer across the interface, and Rashba SOC [11–13]. In the case of superlattices of low-bandwidth  $\text{CaIrO}_3$  and  $\text{SrTiO}_3$ , the mechanism underlying the AMR is a combination of in-plane biaxial magnetic anisotropy, magneto-elastic coupling, and interlayer exchange coupling based on tilted oxygen octahedra with glazer notation ( $a^-a^-c^+$ ) across the constituent layers [13–15]. Despite all these diverse yet concerted efforts, the maximum amplitude of the fourfold AMR signal in  $3d$ - $5d$  heterostructures is limited to 1%. This demands the development of strategies in terms of the choice of constituents and the architecture of the heterostructures that efficiently translate the magnetism into a larger AMR effect.

Here, we have formed superlattice heterostructures of low-bandwidth  $\text{CaIrO}_3$  and severely distorted canted AFM  $\text{CaMnO}_3$ , where both these constituents have the same sense of oxygen octahedra tilts ( $a^-a^-c^+$ )—a conducive factor for interlayer coupling. Thus, a thickness-optimized architecture exhibits an unprecedented fourfold AMR of  $\sim 70\%$ . Two different effects—biaxial anisotropy and spin-flop transition—combine to yield this AMR. The former contributes up to 20% signal as fourfold symmetric sinusoidal AMR, and the latter further increases it by an order of magnitude as well as imposes another unique fourfold symmetric component.

The superlattices  $[(\text{CaMnO}_3)_x/(\text{CaIrO}_3)_y]_z$  ( $x, y =$  number of unit cells (u.c.)/period;  $z =$  repetitions) were prepared by the reflection high-energy electron diffraction-assisted pulsed laser deposition technique. These samples are labeled as  $(\text{M}Ixy)_z$ , where  $M$  and  $I$  refer to  $\text{CaMnO}_3$  and  $\text{CaIrO}_3$  layers, respectively, and categorized based on the period of

\*dsrana@iiserb.ac.in

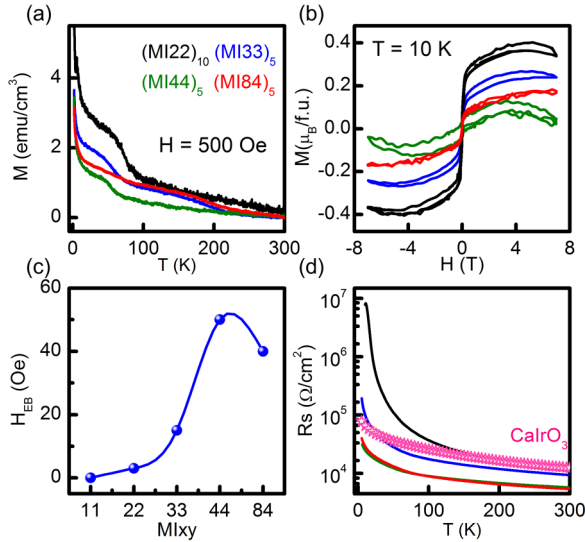


FIG. 1. (a) Temperature, (b) field dependence of magnetization, and (c) the strength of exchange bias field with the varying stacking of  $\text{CaMnO}_3$  and  $\text{CaIrO}_3$  layers in the  $(\text{MI}_{xy})_z$  superlattices. (d) Sheet resistance as a function of temperature for  $(\text{MI}_{xy})_z$  ( $x = y = 2-4$ ) along with  $(\text{MI84})_5$  to elucidate the effect of a larger  $\text{CaMnO}_3$  period.

constituent layers. Details of sample synthesis and characterization methods are appended in the Supplemental Material [16].

Magnetization ( $M$ ) vs temperature and magnetic field ( $H$ ) data of  $(\text{MI}_{xy})_z$  ( $x = y = 2-4$ ) superlattices are plotted in Figs. 1(a) and 1(b). The magnetic transition temperature ( $T_C$ ) and the saturation magnetic moment ( $M_{\text{sat}}$ ) decrease with increasing period. A discernible  $T_C$  of  $\sim 100$  K for  $(\text{MI22})_{10}$  decreases to  $\sim 60$  K for  $(\text{MI44})_5$  and vanishes for higher periods superlattice  $(\text{MI84})_5$ . In  $M$ - $H$  data, a  $M_{\text{sat}}$  of  $\sim 0.4 \mu_B/\text{f.u.}$  for  $(\text{MI22})_{10}$  agrees well with the reported canted AFM state in  $\text{CaIrO}_3/\text{CaMnO}_3$  heterostructures [13,17] [Fig. 1(b)]. Given that  $M_{\text{sat}}$  of the same order manifests in other samples too, the exchange-bias fields ( $H_{\text{EB}}$ ) were measured by performing field-cooled  $M$ - $H$  measurements. Observation of an  $H_{\text{EB}}$  field of 3, 15, 50, and 35 Oe for  $(\text{MI22})_{10}$ ,  $(\text{MI33})_5$ ,  $(\text{MI44})_5$ , and  $(\text{MI84})_5$ , respectively, suggests FM- and AFM-type phases in these superlattices [Fig. 1(c)]. The sheet resistance increases with decreasing  $\text{CaIrO}_3$  period [Fig. 1(d)]. A sharp upturn in resistivity  $< 50$  K is associated with the Mott state, which has been explained in the framework of dimensionality-induced enhancement in correlations  $U$  and charge transfer across the interface [18,19]. Though all the superlattices are in Mott-insulating regime, the resistivity of  $(\text{MI84})_5$  and  $(\text{MI44})_5$  is lower than  $\text{CaIrO}_3$  10 nm film. As  $\text{CaMnO}_3$  is an insulator, while  $\text{CaIrO}_3$  is a semimetal, this lesser resistivity can be explained in context to the larger charge transfer in thicker superlattices promoting double exchange in manganite layer (discussed later).

In superlattices involving manganites, the valence state can be altered at the interfaces through the transfer of charge [20–23]. To explore the microscopic origin of the magnetization and exchange-bias fields in  $\text{CaIrO}_3/\text{CaMnO}_3$  superlattices, the interfacial charge transfer and electronic structure close to the Fermi level were qualitatively visualized

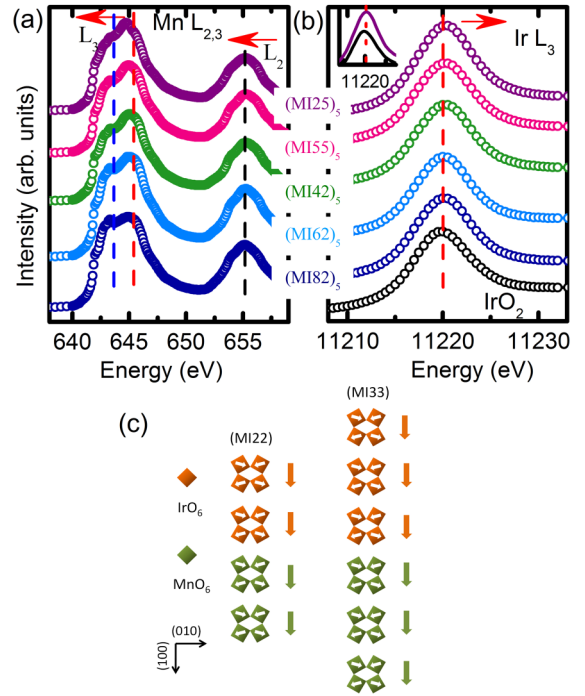


FIG. 2. X-ray absorption spectra around (a) the  $\text{Mn } L_{2,3}$  edge and (b)  $\text{Ir } L_3$  edge for  $(\text{MI}_{xy})_z$  superlattices. The insets depict the comparison of the  $(\text{MI25})_5$  sample with the  $\text{IrO}_2$  reference. (c) Schematic illustrating the spin canting in  $\text{CaIrO}_3$  and  $\text{CaMnO}_3$  layers. Here,  $\text{BO}_6$  planes for  $\text{CaIrO}_3$  and  $\text{CaMnO}_3$  layers are presented in the  $ab$  plane (or in plane). These planes are stacked along  $[001]$ , but for the sake of brevity, the top view of the canted moments and net magnetic moment is presented along two in-plane  $[010]$  and  $[100]$  directions, with reference to the pseudocubic STO  $(100)$  substrate. The length of the arrows showing net magnetic moment does not represent the relative size of the magnetic moment in  $\text{CaIrO}_3$  or  $\text{CaMnO}_3$  layers.

via x-ray absorption spectroscopy (XAS) at the Mn and Ir  $L$  edges [Figs. 2(a) and 2(b)]. Superlattices with 2 u.c. of one constituent and  $> 4$  u.c. of the other constituent were chosen to extract the role of both constituents on charge transfer. The Mn  $2p$  core spectra for all superlattices show a shift in the  $L_3$  edge peak toward lower energy. This suggests the presence of  $\text{Mn}^{3+}$  ions [18,24–26], presumably formed by the transfer of charge from the Ir at the interface. Similarly, the XAS at the Ir  $L$ -edge spectra depicts a shift in the peak toward higher energy values with respect to  $\text{IrO}_2$  reference. This implies that the average Ir valency is  $> +4$  due to the charge transfer with Mn [27,28]. A nearly constant shift in Ir edge for all superlattices suggests that  $\text{CaIrO}_3$  tends to lose only a constant fraction of its charge, i.e., superlattices with thinner  $\text{CaMnO}_3$  layers will receive a large fraction of electrons compared with their counterparts with thicker layers. This electronic reconfiguration at the interface is consistent with the emergence of an anomalous magnetism in the superlattices with 2 u.c. of  $\text{CaMnO}_3$  (see Fig. S4 in the Supplemental Material [16] for more details). These data further suggest that the charge transfer depends on the number of both  $\text{CaIrO}_3$  and  $\text{CaMnO}_3$  layers (and available carriers) and is related to the trends in electrical transport and magnetization of these samples, as explained below.

CaMnO<sub>3</sub> with a severely distorted lattice has a strong affinity for electrons due to its vacant  $e_g$  orbital near the Fermi level. A study on Ce<sup>4+</sup>-doped CaMnO<sub>3</sub> revealed that 2–4% electron doping at the Mn site cants the AFM lattice by 8° and increases the magnetic moments by >1 order of magnitude [29]. This electron doping is like charge-transfer/electron leakage across the interface, as reported in CaRuO<sub>3</sub>/CaMnO<sub>3</sub> heterostructures. Here, the electron leakage into CaMnO<sub>3</sub> decays exponentially from the interface to within the layer [30–33]. As a result, a fraction of Mn<sup>4+</sup> proportional to electron leakage converts to Mn<sup>3+</sup>, which induces a double-exchange-governed largely canted AFM or a weak FM phase at the interface layer. The inner part of the CaMnO<sub>3</sub> layer remains weakly canted, as it coincides with the exponential tail of electron leakage. Both theory and experiments agree on the formation of such a magnetic gradient across the CaMnO<sub>3</sub> layer [30–33]. The CaIrO<sub>3</sub> too presents a canted AFM phase in low dimensions when hetero-interfaced with a distorted lattice, as in  $3d$ - $5d$  heterostructures. All these report as well the magnetization data of present CaIrO<sub>3</sub>/CaMnO<sub>3</sub> samples point toward a canted AFM state for both the constituent layers. The manifestation of  $H_{EB}$  in these samples [Fig. 1(c)] further confirms the magnetic gradient across the interface. An illustration of the direction of canting and moments is presented in Fig. 2(c). The choice of canting the moments in the  $ab$  plane (or in plane) will be discussed in the context of AMR results in later sections.

AMR was measured in three different senses of rotation of the magnetic field with respect to the superlattice plane [34] and calculated as

$$\text{AMR} = \frac{\rho[B(\text{angle})] - \rho[B(\text{angle} = 90^\circ)]}{\rho[B(\text{angle} = 90^\circ)]}. \quad (1)$$

Figure 3(a) depicts three rotation angles, namely,  $\phi$ ,  $\theta$ , and  $\gamma$  with  $H$  rotating in  $xy$ ,  $yz$ , and  $zx$  planes, respectively. A comparison of the  $\phi$ ,  $\theta$ , and  $\gamma$  AMR for (MI22)<sub>10</sub> and (MI33)<sub>5</sub> is elucidated in Figs. 3(b) and 3(c). Here,  $\phi$  AMR exhibits well-defined fourfold sinusoidal oscillations for both these samples. The  $\theta$  and  $\gamma$  AMRs are twofold for (MI22)<sub>10</sub> but have a subtle fourfold component superimposed on a dominant twofold component for (MI33)<sub>5</sub>. The origin of the AMR can be ascertained by comparing these three types and analyzing their dependence on the magnetic field. None of the  $\phi$ ,  $\theta$ , and  $\gamma$  AMRs follows a quadratic dependence on  $B$  (Fig. S5 in the Supplemental Material [16]), which rules out their origin in Lorentz scattering [13]. In addition, a coincident magnitude and phase of  $\theta$  and  $\gamma$  AMRs for (MI22)<sub>10</sub> discards the possibility of either spin Hall MR or  $s$ - $d$  scattering as the underlying mechanisms [34–37].

While large  $\theta$  and  $\gamma$  AMRs of up to ~15% manifest for (MI22)<sub>10</sub>, the most remarkable facets of this paper are unraveled in much-desired fourfold  $\phi$  AMR. Figures 3(d) and 3(e) show the  $\phi$  AMR as a function of layer thickness and their temperature dependences in (MI $x$ y) <sub>$z$</sub>  ( $x = y = 2$ –4) and (MI84)<sub>5</sub>. The (MI22)<sub>10</sub> exhibits  $\phi$  AMR of 70% at 10 K. It reduces to ~3–4% for (MI33)<sub>5</sub> and further declines to 1 and 0.04% for (MI44)<sub>5</sub> and (MI84)<sub>5</sub>, respectively [Fig. 3(e)]. For all the samples, the AMR decreases with increasing temperature and completely disappears around their  $T_C$  in the range of 70–100 K [Fig. 3(e)]. Here,  $\phi$  AMR of 70% in (MI22)<sub>10</sub>

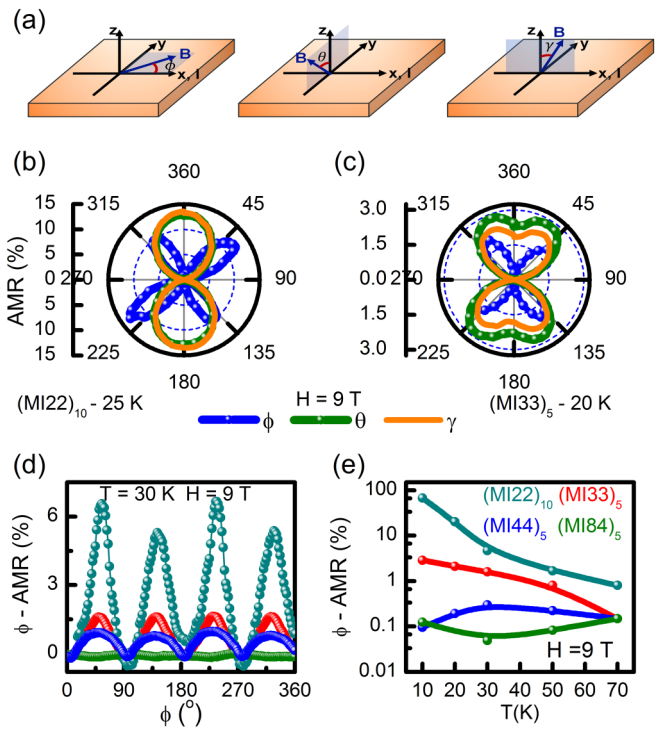


FIG. 3. (a) Schematic illustration of three different rotational geometries to measure the anisotropic magnetoresistance (AMR). Polar plots comparing  $\phi$ ,  $\theta$ , and  $\gamma$  AMRs for (b) (MI22)<sub>10</sub> and (c) (MI33)<sub>5</sub> superlattices. (d) Variation in  $\phi$  AMR at 30 K for (MI $x$ y) <sub>$z$</sub>  ( $x = y = 2$ –4) and (MI84)<sub>5</sub>. (e) Variation in the  $\phi$  AMR amplitude as a function of temperature for  $H = 9$  T.

is unique as (i) it is about two orders of magnitude larger than reported so far in any  $3d$ - $5d$  heterostructures, (ii) it is the largest in complex oxide heterostructures, and (iii) it falls by two orders of magnitude as the period ( $x = y$ ) increases from 2 to 4. This unusual sensitivity of AMR to the constituent layer thickness points toward a different phenomenon promoting the interlayer coupling.

To further pin down the role of individual layers, the  $\phi$  AMR of ((MI $x$ 2) <sub>$z$</sub>  [ $x = 4, 6, \text{ and } 8$ ] and (MI2 $y$ ) <sub>$z$</sub>  [ $y = 4$  and 5] set of heterostructures was studied and the results are presented in Figs. S6–S8 in the Supplemental Material [16]. For the former set, the AMR falls in the narrow range of 0.3–0.6% for all values of  $x$ , while for the latter set, it drops from 1.6% for  $y = 4$  and 0.8% for  $y = 5$ . These values are much smaller than the  $\phi$  AMR of 70% for (MI22)<sub>10</sub>. Hence, it is inferred that a 2 u.c. thickness of both CaIrO<sub>3</sub> and CaMnO<sub>3</sub> layers is critical to obtain a large AMR. A weak magnetism in the canted AFM phase of these superlattices suggests the origin of the AMR to be the domain scattering based on biaxial magnetic anisotropy [13,38–40], which is controlled by the interlayer coupling [41,42]. The strength of this coupling depends on the dimensions of the constituent layers and the interface coupling. In the present case, for example, such coupling is stronger in samples with smaller periods, as in (MI22)<sub>10</sub>. The origin of in-plane biaxial anisotropy and interlayer coupling can be understood as follows.

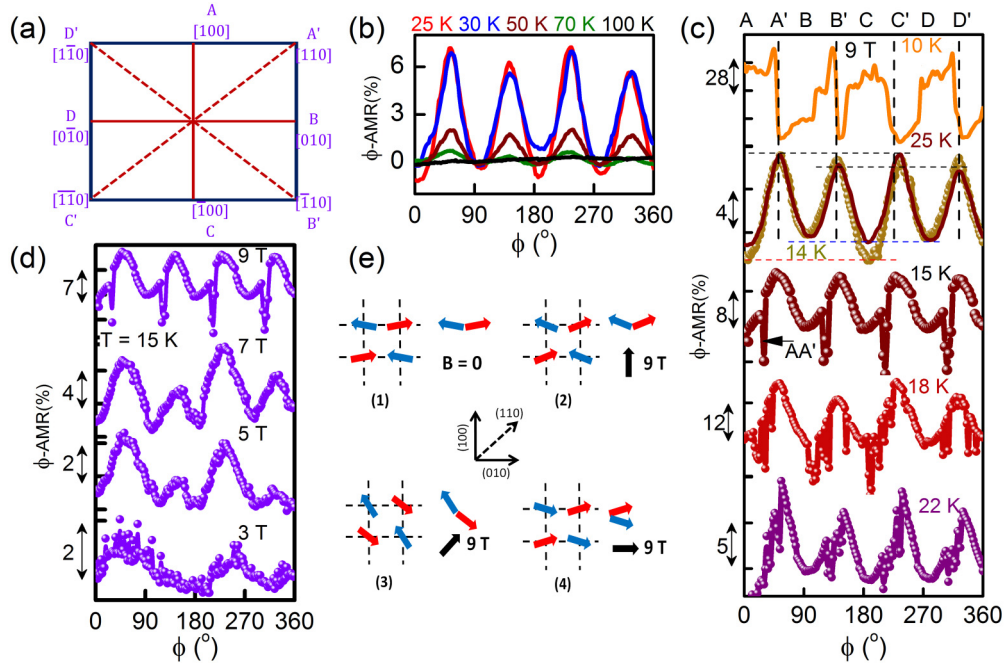


FIG. 4. (a) The  $\langle 100 \rangle$  crystallographic in-plane family of directions is labeled as A, B, C, and D, and the  $\langle 110 \rangle$  family as A', B', C', and D'. (b)  $\phi$ -anisotropic magnetoresistance (AMR) for  $(\text{MI}22)_{10}$  measured at various temperatures in the range of 25–100 K at  $H = 9$  T. (c)  $\phi$  AMR of the  $(\text{MI}22)_{10}$  in the temperature range of 10–20 K for  $H = 9$  T, manifesting the onset of the spin-flop transition at 22 K evident from the additional fourfold symmetry in  $\phi$  AMR. (d) Field dependence of  $\phi$  AMR for  $(\text{MI}22)_{10}$  measured at  $T = 15$  K. (e) Spin arrangement as perceived in relation to the AMR. Spins indicated in two colors (red and blue) correspond to two sublattices of the antiferromagnetic (AFM) order. A canting in AFM order at  $B = 0$  increases in a field of 9 T along the easy (100) axis (1 and 2). This effect is subtle when  $B$  is applied along the (110) hard axis (panel 3). For  $B = 9$  T along (010), the spin-flop arrangement at 10 K is shown in the last panel.

The inter- and intralayer magnetic interaction in  $\text{CaIrO}_3$  layers can be written as [43,44]

$$H_{ij} = J_{ij} \vec{S}_i \cdot \vec{S}_j + \Gamma_{ij} S_i^z S_j^z + \vec{D}_{ij} \cdot (\vec{S}_i \times \vec{S}_j), \quad (2)$$

where  $J_{ij}$  is the isotropic Heisenberg exchange,  $\Gamma_{ij}$  is a symmetric traceless second-rank tensor that describes the symmetric portion of the exchange anisotropy, and  $D_{ij}$  defines the Dzyaloshinskii-Moriya (DM) anisotropy. The asymmetric exchange DM interactions with the  $D$  vector pointing along the  $c$  axis (out-of-plane) cant the moments in  $ab$  in-plane along the  $[100]/[010]$  direction. The latter two terms are essential for in-plane magnetic anisotropy responsible for the manifestation of  $\phi$  AMR [41–43]. Though originally proposed for layered  $\text{Sr}_2\text{IrO}_4$  to explain the strength of interlayer coupling between  $\text{SrIrO}_3$  layers separated by nonmagnetic  $\text{SrO}$  layers, Eq. (2) is also relevant for superlattices where  $\text{CaIrO}_3$  or  $\text{SrIrO}_3$  layers are separated by magnetic or nonmagnetic layers [13,19]. In the present  $\text{CaIrO}_3/\text{CaMnO}_3$  superlattices, the  $\text{CaIrO}_3$  period possesses a larger  $U$  and a canted AFM phase in low dimensions. The  $\text{CaMnO}_3$  too is a canted AFM in the same dimensions. In addition, both these layers have a similar sense of structural distortion of  $(a^-a^+c^+)$  type in low dimensions. This combination of similarity of magnetic phase and structural distortion is a unique attribute and can be argued as a decisive factor for a strong interlayer coupling. This, as stated earlier, is responsible for the biaxial anisotropy and a large fourfold sinusoidal AMR of  $\text{CaIrO}_3/\text{CaMnO}_3$  heterostructures.

Now we turn our attention to some other dynamics of  $\phi$  AMR which are beyond the contribution of biaxial anisotropy in  $(\text{MI}22)_{10}$ . To relate the AMR with crystal orientations, we present in Fig. 4(a) the set of (100) and (110) families of axes along with their labeling in the  $ab$  plane. The sinusoidal  $\phi$  AMR oscillations in the range of 25–100 K [Fig. 4(b)] develop some unique features  $< 22$  K. As scrutinized in very close intervals in the range of 10–22 K, we observe an additional fourfold pattern of AMR kinks superimposed on the sinusoidal pattern while traversing from the  $\langle 100 \rangle$  to the  $\langle 110 \rangle$  family of crystal axes [Fig. 4(c)]. A well-defined fourfold  $\phi$  AMR at 25 K develops a multitude of kinks at 22–18 K, followed by symmetric and sharp fourfold kinks at 15 K. A smooth pattern appears at 14 K which further transforms to a sharp steplike pattern at 10 K along with a reversal in polarity of the peak amplitude. This unprecedented  $\phi$  AMR behavior is complex both in its pattern and amplitude. In a system with biaxial anisotropy, the trough and crest of the  $\phi$  AMR are assigned to the scattering by soft  $\langle 100 \rangle$  (low resistance) and hard  $\langle 110 \rangle$  axes (peak resistance), respectively. There appears to be a transition in the scattering strength from the  $\langle 110 \rangle$  family of directions at 25 K to the  $\langle 100 \rangle$  directions at 14 K [second panel of Fig. 4(c)]. At 25 K, the uneven amplitude of the crests suggests an uneven scattering from the  $\langle 110 \rangle$  family of hard directions, i.e., a larger scattering along A'  $[110]$  and C'  $[\bar{1}\bar{1}0]$  than B'  $[\bar{1}10]$  and D'  $[10\bar{0}]$  [marked by a black dashed line in the second panel of Fig. 4(c)]. In contrast, nearly the same magnitude of troughs suggests the uniform scattering from the  $\langle 100 \rangle$  and  $(010)$  soft directions (marked by

blue dashed lines). At 14 K, however, this behavior reverses. Here, the  $\langle 100 \rangle$  family of soft axes exhibit nonuniformity in the troughs (shown by red dashed lines). This reversal in nonuniformity of scattering is related to a systematic pattern of  $\phi$  AMR kinks in the transition temperatures [Fig. 4(c)]. This anomalous AMR of  $(\text{MI}22)_{10}$  can be explained to arise from competition between pseudospin-lattice (S-L) coupling and field-pseudospin coupling.

The S-L coupling in iridates is given by [41]

$$H_{s-l} = \Gamma_1 \cos(2\alpha)(S_i^x S_j^x - S_i^y S_j^y) + \Gamma_2 \sin(2\alpha)(S_i^x S_j^y + S_i^y S_j^x). \quad (3)$$

Here,  $\Gamma_1$  and  $\Gamma_2$  denote the energy scales of S-L coupling to the distortions along  $\langle 100 \rangle$  and  $\langle 110 \rangle$ , respectively, and  $\alpha$  is the angle between staggered moments and the  $\langle 100 \rangle$  direction. The competition between  $xy$  and  $x^2 - y^2$  quadruple symmetries provides two solutions for  $H = 0$ ;  $\alpha = 45^\circ$  for  $\Gamma_1 > \Gamma_2$ , and  $\alpha = 0$  for  $\Gamma_1 < \Gamma_2$ . The former is observed in  $\text{Sr}_2\text{IrO}_4$  and  $\text{SrIrO}_3/\text{SrTiO}_3$  superlattices, while the latter manifests for  $\text{CaIrO}_3/\text{SrTiO}_3$  heterostructures. The  $\phi$  AMR phase in the present superlattices lags by  $45^\circ$  when compared with  $\text{Sr}_2\text{IrO}_4$  and  $\text{SrIrO}_3/\text{SrTiO}_3$  superlattices [13,45]. The phase lag in  $\text{SrIrO}_3$ - and  $\text{CaIrO}_3$ -based superlattices is due to the different sense of octahedral rotations in their low-dimensional limits. The solution to the present superlattices is at  $\alpha = 0$ , as the minimum of AMR oscillation occurs along the  $\langle 100 \rangle$  directions, like that in  $\text{CaIrO}_3/\text{SrTiO}_3$  superlattices.

The S-L coupling is strong in the vicinity of a magnetic transition and weakens on lowering the temperature [41,44]. The  $\phi$  AMR in  $\text{CaIrO}_3/\text{SrTiO}_3$  superlattices is reported to scale with the strength of S-L coupling and thus peaks around the transition temperature. Contrary to this, in  $\text{CaIrO}_3/\text{CaMnO}_3$  superlattices, the  $\phi$  AMR peaks well below the magnetic transition; for thin superlattices  $(\text{MI}22)_{10}$  and  $(\text{MI}33)_5$ , AMR amplitude monotonically increases with decreasing temperature, showing the maximum AMR at much lower than the magnetic transition, i.e., 10 K. For thick  $(\text{MI}x)_z$  ( $x = 4, 6, \text{ and } 8$ ) superlattices, however, the AMR peaks at the slightly elevated temperature range of 30–50 K (Fig. S9 in the Supplemental Material [16]). This indicates a dominant role of field-pseudospin coupling in addition to the S-L coupling. As the in-plane axis rotates with respect to the field in  $\phi$  AMR measurement, the field-lattice coupling rotates the orthorhombic distortion [41,42]. At low temperatures, however, the stiffness of the lattice weakens the S-L coupling. This tilts the balance in favor of field-pseudospin coupling in the presence of large magnetic moments. A temperature-dependent competition between these two couplings determines the  $\phi$  AMR for  $(\text{MI}22)_{10}$  as (i) reorientation of moments via S-L coupling at high temperature, and (ii) direct coupling of field spins at low temperature when the lattice is rigid but possesses larger moments. For the superlattice having larger canted pseudospin moments, say for  $(\text{MI}22)_{10}$ , the transition from (i) to (ii) onsets at 25 K. Below this temperature, the AMR increases significantly, as evidenced by kinks and sharp steps. These features represent lower resistance and higher magnetization than those corresponding sinusoidal AMR along the soft  $\langle 100 \rangle$  axes. Such a state in AFM/canted AFM can be induced by a spin-flop metamag-

netic transition in high magnetic fields [46] (Fig. 4(d) and Fig. S10 in the Supplemental Material [16]). These kinks become more pronounced upon lowering the temperature from 22 to 15 K while retaining an overall sinusoidal envelope emerging from the S-L coupling. Eventually, at 10 K and in a high field of 9 T, the  $\phi$  AMR oscillations reverse their phase by  $45^\circ$ . This is highlighted by the vertical dashed lines matching the  $\phi$  AMR at (i) 14 and 10 K in a field of 9 T [Fig. 4(c)] and (ii) 10 K in fields of 5 and 9 T (Fig. S11 in the Supplemental Material [16]). The comparison reveals that, as the component of the field gets stronger along  $\langle 110 \rangle$ , a spin-flop metamagnetic transition induces a giant  $\phi$  AMR. The balance shifts dominantly in favor of field-pseudospin coupling that prevents the restoration of the originally sinusoidal resistance.

Metamagnetic transitions are known to occur in manganites as well as in iridates [41,43,47,48]. In half-doped manganites, a sharp steplike metamagnetic transition melts an AFM charge-ordered insulating state into a FM metallic state. There are either single- or multiple-steplike metamagnetic transitions that are facilitated via large A-site quenched disorder or slight B-site doping or structural defects. In iridates, dimensionality- and lattice-distortion-dependent metamagnetic transitions have been demonstrated in layered systems [41,43]. For example, in  $\text{Sr}_2\text{IrO}_4$ , a spin-flop metamagnetic transition is found to be a function of the S-L coupling energetics [41]. A stronger interlayer coupling is the theoretical basis of the spin-flop transition since the coupling strength changes from  $\text{Sr}_2\text{IrO}_4$  to  $\text{Sr}_3\text{Ir}_2\text{O}_7$  [43]. In the present  $\text{CaIrO}_3/\text{CaMnO}_3$  superlattices, the resistance oscillations arise from an oscillating magnetic moment with respect to crystallographic axis embedded in a system with in-plane biaxial magnetic anisotropy. The sharp kink- and steplike transitions are superimposed on these oscillations—inducing an additional large component  $\phi$  AMR—and have their origin in spin-flop metamagnetic transition. A relation of the pseudospin arrangement perceived to corroborate with the crest and trough of sinusoidal AMR and the spin-flop AMR is illustrated in Fig. 4(e). The canting angle and magnetic moment increase upon application of a field of 9 T along the  $\langle 100 \rangle$  easy axis. The canting effect is subtle for the field along  $\langle 110 \rangle$  hard axes (for brevity, the AFM spin arrangement is rotated along the direction of the field). Larger canted moments along  $\langle 100 \rangle$  translate into smaller resistivity than that along the  $\langle 110 \rangle$  family of hard axes. A spin-flop transition at 10 K in a field of 9 T is also illustrated in Fig. 4(e). In this case, larger moments of the spin-flop phase are responsible for a large kink/steplike large AMR.

Finally, we emphasize that the choice of the  $3d$  compound is the key to yielding the effective interlayer coupling and distortion required to tune a large  $\phi$  AMR. In the case of the  $\text{CaIrO}_3/\text{SrTiO}_3$  superlattices, the  $(a^-a^-c^+)$  octahedral distortions in the  $\text{CaIrO}_3$  layers propagate into the mediating  $\text{SrTiO}_3$  layer, provided the  $\text{SrTiO}_3$  layer consists of only 1 u.c. [13]. In contrast, in the present  $\text{CaIrO}_3/\text{CaMnO}_3$  superlattices, this distortion propagates into the mediating  $\text{CaMnO}_3$  layer as thick as 8 u.c. In the dimensional limit of a few unit cells, both  $\text{CaMnO}_3$  and  $\text{CaIrO}_3$  are orthorhombically distorted with the same octahedral rotation pattern  $(a^-a^-c^+)$  and similar in-plane DM-type canted AFM phase [13,49]. This structural similarity between the two constituents enhances

the CaIrO<sub>3</sub> interlayer coupling and results in a large biaxial anisotropy.

To sum up, the CaIrO<sub>3</sub>/CaMnO<sub>3</sub> superlattice shows an unprecedented AMR of  $\sim 70\%$ , utilizing two key factors: a strong biaxial anisotropy and a spin-flop metamagnetic transition. Combined control of tilt pattern and superlattice construction is demonstrated to optimize the biaxial magnetic anisotropy, the interlayer coupling mediated by a thick layer, and the field-pseudospin coupling. All these facets coalesce constructively to maximize the transport anisotropies in *3d-5d* superlattices. This proof-of-concept study is set to introduce avenues for designing highly sensitive AMR readout devices for emerging AFM spintronics.

D.S.R. thanks the Department of Science and Technology (DST) Nanomission for financial support under Research Project No. SM/NM/NS-84/2016 and the Science and Engineering Research Board Technology, New Delhi, under the Project No. CRG/2020/002338. M.V. acknowledges the DST, India, for the INSPIRE faculty award (DST/INSPIRE/04/2017/003059). XAS measurements were performed at UC San Diego in a search for materials for spin-torque oscillators conducted by Quantum Materials for Energy Efficient Neuromorphic Computing, an Energy Fron-

tier Research Center funded by the U.S. Department of Energy (DOE), Office of Science, Basic Energy Sciences under Award No. DE-SC0019273. This paper used resources of the Advanced Photon Source (29ID for soft XAS and 4-ID-D for hard XAS), a DOE Office of Science User Facility operated for the DOE Office of Science by Argonne National Laboratory under Contract No. DE-AC02-06CH11357, with additional support by the National Science Foundation under Grant No. DMR-0703406. Extraordinary facility operations were supported in part by the DOE Office of Science through the National Virtual Biotechnology Laboratory, a consortium of DOE national laboratories focused on the response to COVID-19, with funding provided by the Coronavirus CARES Act. Authors thank Mr. G. L. Prajapati and Mr. Manoj Prajapat for their help in performing magnetization, transport and x-ray diffraction characterizations as well as R. Aniol for transmission electron microscopy (TEM) specimen preparation. Furthermore, the use of the HZDR Ion Beam Center TEM facilities and the funding of TEM Talos by the German Federal Ministry of Education of Research (Grant No. 03SF0451) in the framework of the Helmholtz Energy Materials Characterization Platform are acknowledged.

M.V. and S.S. contributed equally to this paper.

- 
- [1] P. Němec, M. Fiebig, T. Kampfrath, and A. V. Kimel, *Nat. Phys.* **14**, 229 (2018).
- [2] L. Šmejkal, Y. Mokrousov, B. Yan, and A. H. MacDonald, *Nat. Phys.* **14**, 242 (2018).
- [3] T. Jungwirth, J. Sinova, A. Manchon, X. Marti, J. Wunderlich, and C. Felser, *Nat. Phys.* **14**, 200 (2018).
- [4] M. B. Jungfleisch, W. Zhang, and A. Hoffmann, *Phys. Lett. A* **382**, 865 (2018).
- [5] V. Baltz, A. Manchon, M. Tsoi, T. Moriyama, T. Ono, and Y. Tserkovnyak, *Rev. Mod. Phys.* **90**, 015005 (2018).
- [6] T. Jungwirth, X. Marti, P. Wadley, and J. Wunderlich, *Nat. Nano.* **11**, 231 (2016).
- [7] W. Witzczak-Krempa, G. Chen, Y. B. Kim, and L. Balents, *Annu. Rev. Condens. Matter Phys.* **5**, 57 (2014).
- [8] J. G. Rau, E. K.-H. Lee, and H.-Y. Kee, *Annu. Rev. Condens. Matter Phys.* **7**, 195 (2016).
- [9] L. Zhang, B. Pang, Y. B. Chen, and Y. Chen, *Crit. Rev. Solid State Mater. Sci.* **43**, 367 (2018).
- [10] M. Masuko, J. Fujioka, M. Nakamura, M. Kawasaki, and Y. Tokura, *APL Mater.* **7**, 081115 (2019).
- [11] K. Huang, L. Wu, M. Wang, N. Swain, M. Motapothula, Y. Luo, K. Han, M. Chen, C. Ye, A. J. Yang, H. Xu, D. C. Qi, A. T. N'Diaye, C. Panagopoulos, D. Primetzhofer, L. Shen, P. Sengupta, J. Ma, Z. Feng, C. W. Nan, and X. R. Wang, *Appl. Phys. Rev.* **7**, 011401 (2020).
- [12] D. Yi, J. Liu, S. L. Hsu, L. Zhang, Y. Choi, J. W. Kim, Z. Chen, J. D. Clarkson, C. R. Serrao, E. Arenholz, P. J. Ryan, H. Xu, R. J. Birgeneau, and R. Ramesh, *Proc. Natl. Acad. Sci. USA* **113**, 6397 (2016).
- [13] Z. S. Lim, C. Li, X. Chi, G. J. Omar, H. H. Ma, Z. Huang, S. Zeng, P. Yang, T. Venkatesan, A. Rusydi, S. J. Pennycook, and A. Ariando, *Nano Lett.* **20**, 1890 (2020).
- [14] A. M. Glazer, *Acta. Cryst.* **B28**, 3384 (1972).
- [15] A. M. Glazer, *Acta. Cryst.* **A31**, 756 (1975).
- [16] See Supplemental Material at <http://link.aps.org/supplemental/10.1103/PhysRevB.105.L020402> for additional data and details on the experiments and data analysis.
- [17] Z. S. Lim, C. Li, Z. Huang, X. Chi, J. Zhou, S. Zeng, G. J. Omar, Y. P. Feng, A. Rusydi, S. J. Pennycook, T. Venkatesan, and A. Ariando, *Small* **16**, 2004683 (2020).
- [18] J. Nichols, X. Gao, S. Lee, T. C. Meyer, J. W. Freeland, V. Lauter, D. Yi, J. Liu, D. Haskel, J. R. Petrie, E. J. Guo, A. Herklotz, D. Lee, T. J. Ward, G. Eres, M. R. Fitzsimmons, and H. N. Lee, *Nat. Comms.* **7**, 12721 (2016).
- [19] J. Matsuno, K. Ihara, S. Yamamura, H. Wadati, K. Ishii, V. V. Shankar, H. Y. Kee, and H. Takagi, *Phys. Rev. Lett.* **114**, 247209 (2015).
- [20] J. B. Goodenough, *Phys. Rev.* **100**, 564 (1955).
- [21] R. K. Sahu, Z. Hu, M. L. Rao, S. S. Manoharan, T. Schmidt, B. Richter, M. Knupfer, M. Golden, J. Fink, and C. M. Schneider, *Phys. Rev. B* **66**, 144415 (2002).
- [22] H. L. Feng, M. P. Ghimire, Z. Hu, S. C. Liao, S. Agrestini, J. Chen, Y. Yuan, Y. Matsushita, Y. Tsujimoto, Y. Katsuya, M. Tanaka, H. J. Lin, C. T. Chen, S. C. Weng, M. Valdivares, K. Chen, F. Baudelet, A. Tanaka, M. Greenblatt, L. H. Tjeng, and K. Yamaura, *Phys. Rev. Materials* **3**, 124404 (2019).
- [23] E. Shimshoni, N. Andrei, and A. Rosch, *Phys. Rev. B* **68**, 104401 (2003).
- [24] P. Orgiani, A. Galdi, C. Aruta, V. Cataudella, G. De Filippis, C. A. Perroni, V. Marigliano Ramaglia, R. Ciancio, N. B. Brookes, M. Moretti Sala, G. Ghiringhelli, and L. Maritato, *Phys. Rev. B* **82**, 205122 (2010).
- [25] D. H. Kim, S. M. Lee, S. Kolesnik, B. Dabrowski, B.-G. Park, J.-Y. Kim, J. Lee, B. I. Min, and J.-S. Kang, *J. Appl. Phys.* **107**, 09E137 (2010).

- [26] S. Pal, S. Govinda, M. Goyal, S. Mukherjee, B. Pal, R. Saha, A. Sundaresan, S. Jana, O. Karis, J. W. Freeland, and D. D. Sarma, *Phys. Rev. B* **97**, 165137 (2018).
- [27] M. A. Laguna-Marco, P. Kayser, J. A. Alonso, M. J. Martínez-Lope, M. van Veenendaal, Y. Choi, and D. Haskel, *Phys. Rev. B* **91**, 214433 (2015).
- [28] A. Minguzzi, O. Lugaresi, E. Achilli, C. Locatelli, A. Vertova, P. Ghigna, and S. Rondinini, *Chem. Sci.* **5**, 3591 (2014).
- [29] L. Vistoli, W. Wang, A. Sander, Q. Zhu, B. Casals, R. Cichelero, A. Barthélémy, S. Fusil, G. Herranz, S. Valencia, R. Abrudan, E. Weschke, K. Nakazawa, H. Kohno, J. Santamaria, W. Wu, V. Garcia, and M. Bibes, *Nat. Phys.* **15**, 67 (2019).
- [30] B. R. K. Nanda, S. Satpathy, and M. S. Springborg, *Phys. Rev. Lett.* **98**, 216804 (2007).
- [31] C. He, A. J. Grutter, M. Gu, N. D. Browning, Y. Takamura, B. J. Kirby, J. A. Borchers, J. W. Kim, M. R. Fitzsimmons, X. Zhai, V. V. Mehta, F. J. Wong, and Y. Suzuki, *Phys. Rev. Lett.* **109**, 197202 (2012).
- [32] P. Pandey, R. Rana, and D. S. Rana, *Europhys. Lett.* **109**, 38005 (2015).
- [33] P. Pandey, T. Das, R. Rana, J. B. Parmar, S. Bhattacharyya, and D. S. Rana, *Nanoscale* **7**, 3292 (2015).
- [34] S. Vélez, V. N. Golovach, A. Bedoya-Pinto, M. Isasa, E. Sagasta, M. Abadía, C. Rogero, L. E. Hueso, F. S. Bergeret, and F. Casanova, *Phys. Rev. Lett.* **116**, 016603 (2016).
- [35] G. Peramaiyan, R. Sankar, I. P. Muthuselvam, and W.-L. Lee, *Sci. Rep.* **8**, 6414 (2018).
- [36] T. S. Suraj, G. J. Omar, H. Jani, M. M. Juvaaid, S. Hooda, A. Chaudhuri, A. Rusydi, K. Sethupathi, T. Venkatesan, A. Ariando, and M. S. Ramachandra Rao, *Phys. Rev. B* **102**, 125145 (2020).
- [37] H. Nakayama, M. Althammer, Y.-T. Chen, K. Uchida, Y. Kajiwara, D. Kikuchi, T. Ohtani, S. Geprägs, M. Opel, S. Takahashi, R. Gross, G. E. W. Bauer, S. T. B. Goennenwein, and E. Saitoh, *Phys. Rev. Lett.* **110**, 206601 (2013).
- [38] P. Wadley, B. Howells, J. Železný, C. Andrews, V. Hills, R. P. Campion, V. Novák, K. Olejník, F. Maccherozzi, S. S. Dhesi, S. Y. Martin, T. Wagner, J. Wunderlich, F. Freimuth, Y. Mokrousov, J. Kuneš, J. S. Chauhan, M. J. Grzybowski, A. W. Rushforth, K. W. Edmonds, B. L. Gallagher, and T. Jungwirth, *Science* **351**, 587 (2016).
- [39] N. Lee, E. Ko, H. Y. Choi, Y. J. Hong, M. Nauman, W. Kang, H. J. Choi, Y. J. Choi, and Y. Jo, *Adv. Mater.* **30**, 1805564 (2018).
- [40] H. Wang, C. Lu, J. Chen, Y. Liu, S. L. Yuan, S. W. Cheong, S. Dong, and J. M. Liu, *Nat. Commun.* **10**, 2280 (2019).
- [41] H. Liu and G. Khaliullin, *Phys. Rev. Lett.* **122**, 057203 (2019).
- [42] J. Porras, J. Bertinshaw, H. Liu, G. Khaliullin, N. H. Sung, J.-W. Kim, S. Francoual, P. Steffens, G. Deng, M. M. Sala, A. Efimenko, A. Said, D. Casa, X. Huang, T. Gog, J. Kim, B. Keimer, and B. J. Kim, *Phys. Rev. B* **99**, 085125 (2019).
- [43] J. W. Kim, Y. Choi, J. Kim, J. F. Mitchell, G. Jackeli, M. Daghofer, J. van den Brink, G. Khaliullin, and B. J. Kim, *Phys. Rev. Lett.* **109**, 037204 (2012).
- [44] Y. F. Nie, P. D. C. King, C. H. Kim, M. Uchida, H. I. Wei, B. D. Faeth, J. P. Ruf, J. P. C. Ruff, L. Xie, X. Pan, C. J. Fennie, D. G. Schlom, and K. M. Shen, *Phys. Rev. Lett.* **114**, 016401 (2015).
- [45] I. Fina, X. Marti, D. Yi, J. Liu, J. H. Chu, C. Rayan-Serrao, S. Suresha, A. B. Shick, J. Železný, T. Jungwirth, J. Fontcuberta, and R. Ramesh, *Nat. Commun.* **5**, 4671 (2014).
- [46] T. Wu, C. H. Wang, G. Wu, D. F. Fang, J. L. Luo, G. T. Liu, and X. H. Chen, *J. Phys.: Condens. Matter* **20**, 275226 (2008).
- [47] D. S. Rana, D. G. Kuberkar, and S. K. Malik, *Phys. Rev. B* **73**, 064407 (2006).
- [48] R. Mahendiran, A. Maignan, S. Hebert, C. Martin, M. Hervieu, B. Raveau, J. F. Mitchell, and P. Schiffer, *Phys. Rev. Lett.* **89**, 286602 (2002).
- [49] J. Klarbring and S. I. Simak, *Phys. Rev. B* **97**, 024108 (2018).